SI Appendix

Supporting Information for the article:

Discovery of fairy circles in Australia supports self-organization theory

Stephan Getzin, Hezi Yizhaq, Bronwyn Bell, Todd E. Erickson, Anthony C. Postle, Itzhak Katra, Omer Tzuk, Yuval R. Zelnik, Kerstin Wiegand, Thorsten Wiegand, and Ehud Meron

Supporting Methods

Supporting Figures S1-S5

Supporting Tables S1-S5

Supporting References

Supporting Methods

Soil analysis

Particle size distribution (PSD) over the range of 0.08 to 2000 μm was obtained from a high-resolution laser diffractometer (ANALYSETTE 22 MicroTec Plus). Each sample was dispersed by sonication (at 38 kHz) in a Na-hexametaphosphate solution (0.5%), then transferred to a fluid module of the instrument containing deionized water, and subjected to three consecutive 1 min runs at a medium pump speed of 6 l/min. The data were processed using the Mie scattering model (RI = 1.56, AC = 0.01) with an error < 5.0%. The MaS control software was employed to determine the statistical parameters. Soil organic matter (SOM) was determined as the weight ratio by the dry combustion method (375°C for 17 h). Electrical conductivity (EC) and acidity (pH) were measured by specific electrodes in solutions after extraction of the soil water from the samples.

Mineralogical composition was obtained by phase analysis of the samples using the X-ray powder diffraction (XRPD) method. The data were collected on Philips 1050/70 powder diffractometer, with a graphite monochromator on diffracted beam providing Kp radiation (=1.541 Å) and operating at v =40 kV, I = 30 mA. Samples of 1 g were scanned within 5-60° 2-theta range by the step scanning mode with a step of 0.05° and time 1 sec per step. For detailed analysis of clay minerals, the slow scan was carried out within an angle range of 5-15°, with the step 0.02°, and 5 sec per step. Phase identification was performed by using the Bede ZDS computer search/match program coupled with the ICDD (International Centre for Diffraction Data) Powder Diffraction File database. The References Intensities Ratio (RIR) method was used to determine the concentrations of the crystalline components. The integral intensities of main peaks were taken for computation. Elemental analysis was performed by the X-Ray Fluorescence (XRF) method using XRF Spectrometer, PANalytical Co., model Axios [WDXRF (wavelength dispersive), 1 kW]. Omnian software was used for quantitative analysis. Hydrological parameters were calculated following in-situ measures by the disk-infiltrometer (Decagon Devices, Inc.) method, which measures the cumulative volume of water that infiltrates over specified time intervals. Initial infiltration (Ii) and final infiltration (If) were derived from the infiltration flux curve. The hydraulic conductivity (k) was calculated as C/A, where C is the coefficient of the infiltration cumulative curve, and A is a van Genuchten parameter of a given soil type and soil-water suction pressure.

The soil crusts from a termite mound and physical crusts from gap centers were examined for chemical composition and morphology by Scanning Electron Microscope and Energy Dispersive X-Ray Spectrometer (SEM/EDS) (Quanta 200, FEI). The samples were analyzed under 25.0 kV with magnification scale of X5000 (Fig. S4B,D).

Equations used in the process-based model

The model we studied is based on an earlier model introduced by Gilad et al. (1), after being modified to describe the particular characteristics of the Australian FC ecosystem. It consists of the following equations for the areal densities of the vegetation biomass (B), soil water (W), and surface water (H):

$$\partial_T B = G_B B\left(1 - \frac{B}{K}\right) - MB + D_B \nabla^2 B \qquad (1a)$$

$$\partial_T W = IH - L_W W - G_W W + D_W \nabla^2 W \qquad (1b)$$

$$\partial_T H = P - IH - L_H H + D_H \nabla^2 H^2 \qquad (1c)$$

Here T is time in units of years, $\nabla^2 = \partial_X^2 + \partial_Y^2$ is the Laplacian in the (X, Y) plane, and

$$L_W = \frac{N_W}{1+R_W B/K}, \quad L_H = \frac{N_H}{1+R_H B/K}, \quad I = A\frac{B+Qf}{B+Q},$$

$$G_B = \Lambda W(1+EB)^2, \quad G_W = \Gamma B(1+EB)^2 .$$

The rest of the parameters in the model equations, and the numerical values we used here, are presented below in Table S4.

To eliminate redundant parameters we transformed the model equations (1) to a dimensionless form by rescaling the variables and parameters. The dimensionless model equations read

$$\partial_t b = g_b b(1-b) - b + \nabla^2 b \qquad (2a)$$

$$\partial_t w = \mathcal{J} h - l_w w - g_w w + \delta_w \nabla^2 w \qquad (2b)$$

$$\partial_t h = p - \mathcal{J} h - l_h h + \delta_h \nabla^2 h^2, \qquad (2c)$$

where

$$l_w = \frac{\nu_w}{1+R_w b}, \quad l_h = \frac{\nu_h}{1+R_h b}, \quad \mathcal{J} = \alpha\frac{b+qf}{b+q},$$

$$g_b = w(1+\eta b)^2, \quad g_w = \gamma b(1+\eta b)^2 .$$

The bare-soil solution of (2) is given by

$$b_0 = 0, \quad w_0 = \frac{\alpha f p}{\nu_w(\alpha f+\nu_h)}, \quad h_0 = \frac{p}{\alpha f+\nu_h}.$$

Using a linear stability analysis of this solution and going back to dimensional quantities, we find that the bare-soil solution is stable in the range $0 < P < P_2$, where

$$P_2 = \frac{MN_W}{\Lambda}\left(1+\frac{N_H}{Af}\right). \qquad (3)$$

Note that N_H/Af is the ratio of the surface-water evaporation rate to the surface-water infiltration rate in bare soil. In the present context this quantity is not negligible and can significantly extend the stability range of the bare-soil state to higher precipitation values. In addition to the stationary uniform bare-soil solution, equations (1) also have a stationary uniform vegetation solution and stationary periodic solutions as the bifurcation diagram in Fig. 4 shows.

Supporting Figures

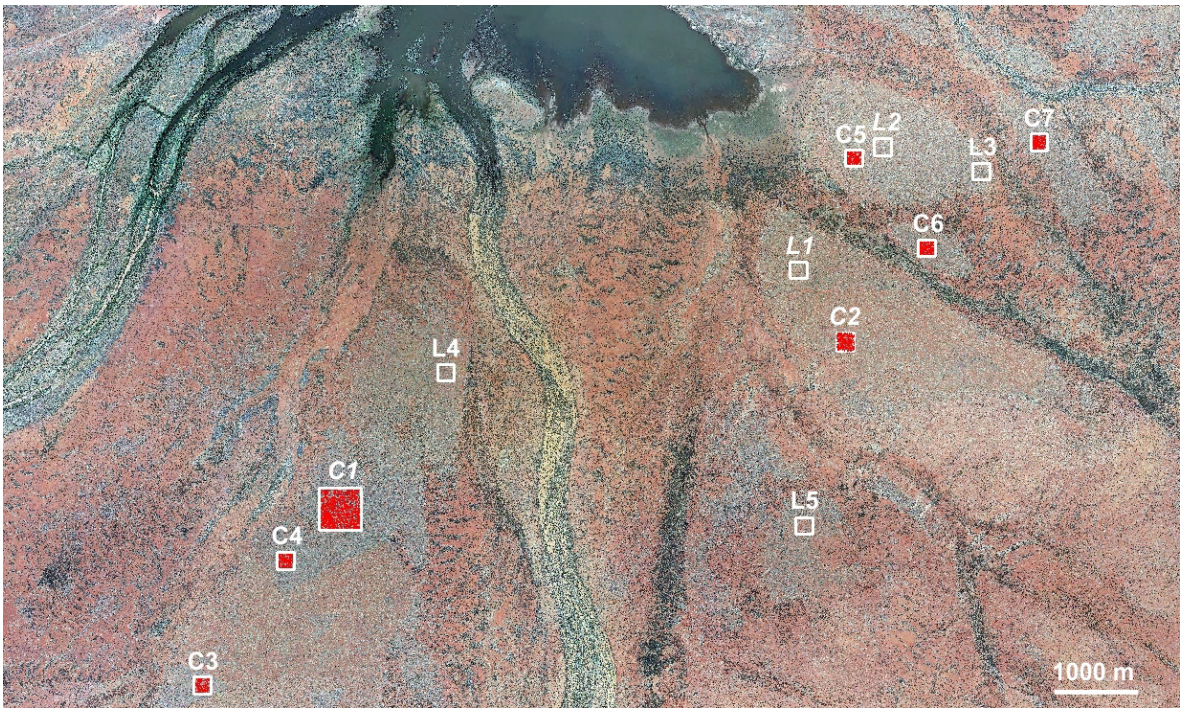

Figure S1. Location of all analyzed study plots. C = plots dominated by 'fairy circle' (gap) patterns, L = plots with transitions to labyrinth patterns. Labels in italics indicate field sites. Except for the plot C1 (500 m × 500 m) and the plot C2 (GPS-mapping of termite and ant nests on an area of 210 m × 210 m), all other analyzed plots have a size of 200 m × 200 m. Coordinates of field plots, C1: 23°24'3"S, 119°51'6"E; C2: 23°22'50"S, 119°54'37"E; L1: 23°22'22"S, 119°54'17"E; L2: 23°21'33"S, 119°54'52"E.

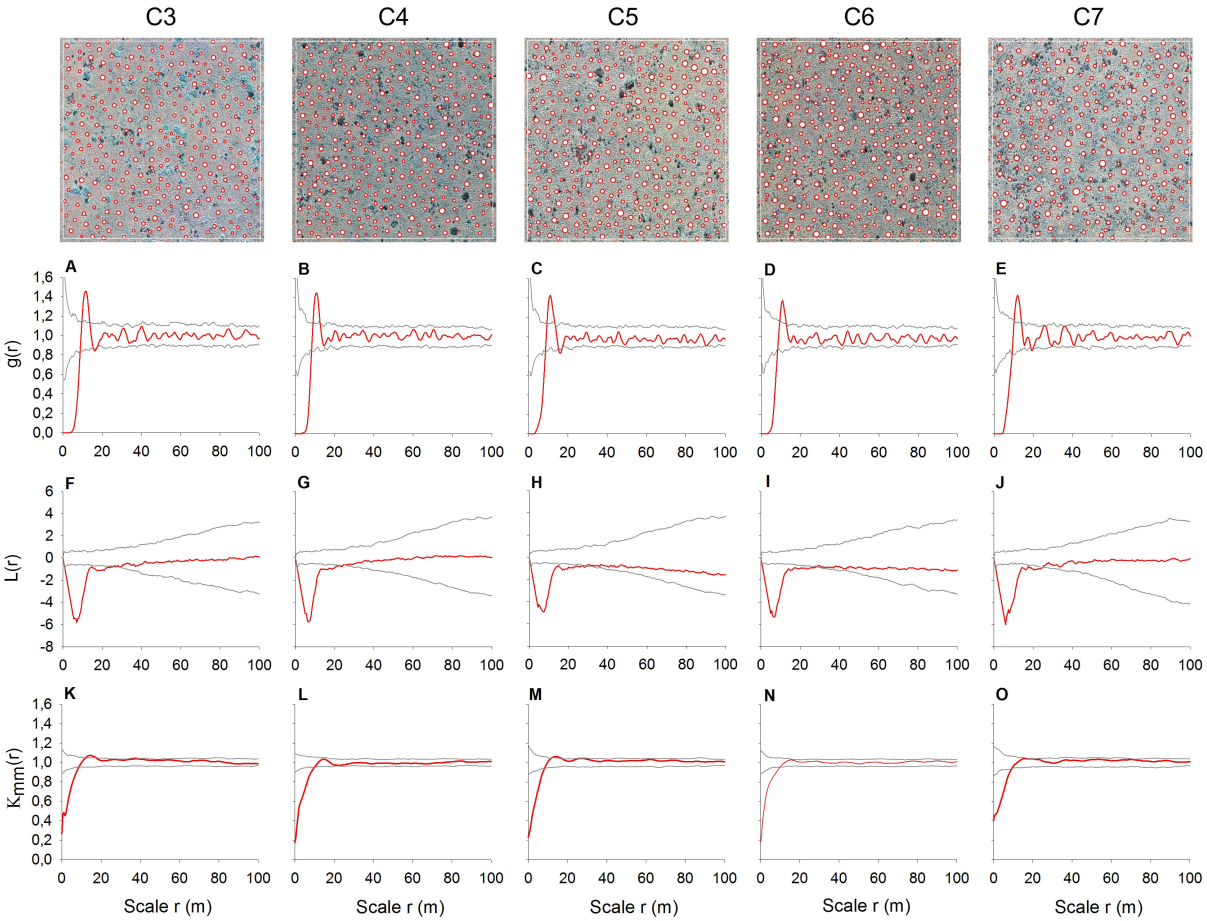

Figure S2. Spatial analysis of five additional aerial images with typical FC patterns. The plot size is 200 m × 200 m. The spatial patterns were contrasted to null models using the pair-correlation function (A–E), *L*-function (F–J), and mark-correlation function (K–O). Patterns are regular and aggregated at circular neighborhood scales *r* if the red line of $g(r)$ or $L(r)$ is below the lower and above the upper grey lines of the simulation envelopes, respectively. Due to its cumulative nature, the *L*-function is particularly suitable to assess departure from a homogeneous random distribution at larger scales. Circle areas are negatively and positively correlated if the red line of $k_{mm}(r)$ is below and above the simulation envelopes, respectively. Approximately 95% simulation envelopes were constructed using the 5th-lowest and 5th-highest value of 199 Monte Carlo simulations of the null models (for details see Materials and Methods).

Figure S3. Differences between soil-surface temperatures at gap centers and peripheries and its effect on plant vitality. Soil-surface temperature at noon reached as much as 75°C in the gap center (A) when ambient air temperature was 45°C. At the gap periphery under dead grass tussocks (B), soil-surface temperature was 67°C and under alive green tussocks (C) only 53°C. While gap centers are subject to extreme thermal stress and high evaporation rates, living spinifex vegetation with its shading effect may decrease soil-surface temperatures by as much as 22°C in comparison to the gap center. These temperature differences were less pronounced on partly cloudy days with ambient air temperature of only 40°C at noon. Gap centers then had a temperature of only 54°C and soil under live tussocks had 43°C. The high

thermal stress and associated high evaporation, combined with significant soil compaction (a hard clay-rich layer) following rainfall led to adverse conditions for plant growth in the gap center where grasses cannot survive (D, E) while grasses at the periphery benefit from shading, water runoff, and increased infiltration (F). Individual grass tussocks, however, may locally survive under more porous sandy conditions which occurred often at transitions from labyrinthine to gap patterns when gaps were forming after recovery from fire (G). Images (D) and (E) show the circular arrangement of individual spinifex plants around the gap. The scale bar in the images is 0.5 m. None of these gaps showed any signs of termite activity.

To demonstrate in a very simple experiment that the FCs function as water source for runoff (H), we irrigated the 1 m^2 center of a gap in the study area C1 with 40 liters of water, which approximately equals a heavy rainfall event of 40 mm. The results show that infiltration was very low in the center (central arrow) and that water immediately moved towards the gap edges where it either stayed at closed barriers of coalesced spinifex grasses (right arrow) or moved out into the vegetation matrix (left arrow) if plants did not form a closed barrier. Closed barriers of individual spinifex plants strongly benefit from the directional flow (arrow) of water runoff from the gap center to the periphery (I). Infiltration rates of the gap, periphery, and vegetation matrix are presented below in Table S2.

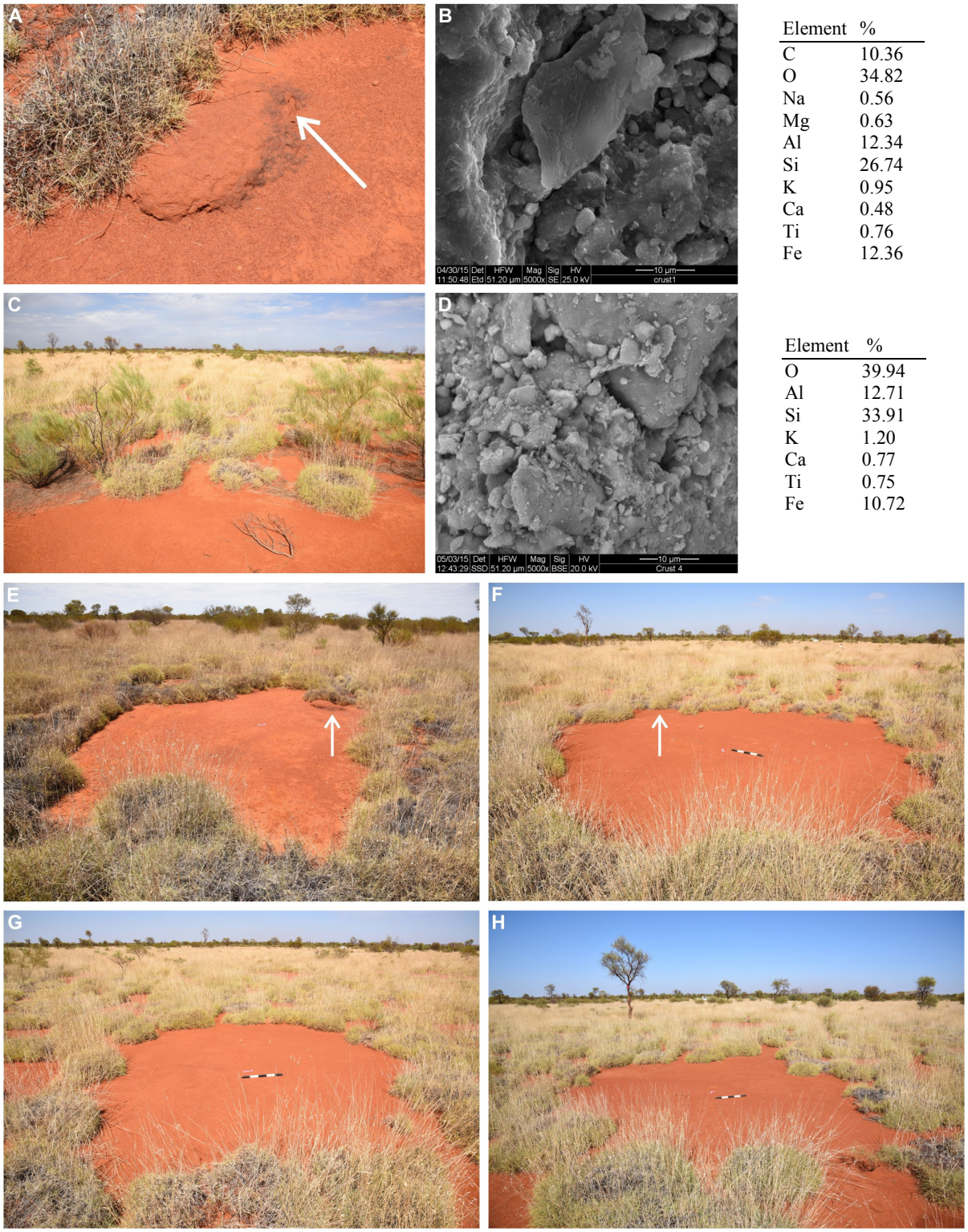

Element	%
C	10.36
O	34.82
Na	0.56
Mg	0.63
Al	12.34
Si	26.74
K	0.95
Ca	0.48
Ti	0.76
Fe	12.36

Element	%
O	39.94
Al	12.71
Si	33.91
K	1.20
Ca	0.77
Ti	0.75
Fe	10.72

Figure S4. Gap characteristics with and without termite signs. Crust sample (arrow) from termite mound (A) and image of this sample from scanning electron microscope (B). The same analysis was undertaken for physical crusts which were unaffected by termite mounds (C,D). SEM-EDS-chemical analysis of elemental mass fraction with high resolution electron microscopy shown in the tables revealed that the mechanical crusts found in the gaps were only the result of mechanical weathering/impact of rainfall drops and not the remnants of eroded termite mounds because the crust sample with the termite mound has additional clays and metal oxides (Na, Mg) which are likely brought up by the mound-building termites from

deeper soil layers to the surface (2) and concentrated to form a hard dark crust. View on a gap (E) with one small termite pavement mound at the gap edge (arrow) where the crust sample (A,B) has been taken from. The field-measured mean diameter of this gap was 3.08 m. View on a large gap (4.90 m) where only one small termite foraging hole (arrow) on the flat surface was found (F). Images of two typical FCs without signs of termite activity (G,H). The diameters of these gaps without termite sign were 3.85 m (G) and 4.95 m (H), respectively. The scale bar in the images is 0.5 m. These results show that the large diameters of the gaps cannot be due to termite activity (see also below, Table S3). Vegetation-free patches resulting from erosion of pavement mounds of termite species such as *Drepanotermes rubriceps* or *D. perniger*, species that occur in the study area, are known to cause rather small gaps with mean diameters of approximately 1 m, and in this case the mound erodes in the center of the patch (3). The newly described FCs here have comparatively large diameters (partly exceeding 6-7 m) and in the majority of cases no signs of termite activity at all. If present, neither the size of termite signs (i.e. 30 cm high mound *vs*. foraging hole on flat surface) nor their typical position at the gap edge can thus explain the size and shape of the Australian FCs. The size and shape indicate a consequence of vegetation self-organization where individual plants arrange themselves in a circle to optimize their access to water runoff from the gap center (Fig. S3).

Figure S5. Investigating termite and ant activity. View on a gap with a hard clay layer (A) in the field plot C2, which burnt in early November, 2014, a few weeks before field measurements were taken in December. All signs of termite and ant nests were clearly visible (B) and have been GPS-mapped on an area of 210 m × 210 m (see Fig. 5). In the foreground of (B), the round nest entrance of the ant species *Melophorus bagoti* can be seen (C). In the background, low mounds and rounded pavement mounds can be seen which belong to termite species such as *Drepanotermes rubriceps* and *Tumulitermes hastilis*. Neither these ants nor the termites were attacking the spinifex grass and the clipping of culms by e.g. *T. hastilis* (D) is part of the normal recycling process when dead plant material is reverted to the nutrient pool of the soil (4-6). Excavations around several isolated healthy *Triodia* tussocks (E) and along the edges of gap peripheries (F) did not show any sign of termite galleries, indicating that the vital plants in the grassland were not affected by termites.

Supporting Tables

Table S1. Summary of the main findings of spatial analyses presented in Figs. 3, 5 and Fig. S2.

	C1	C2	C3	C4	C5	C6	C7	Model Australia	Namibia G1
Number of fairy circles per hectare	64.2	74.4	69.5	78.0	78.0	77.5	67.5	61.4	43.2
Mean diameter of circles (m)	3.32	3.87	3.39	3.59	3.86	4.11	3.98	3.86	5.91
Minimum diameters of circles (m)	2.01	2.08	2.01	2.01	2.01	2.24	2.24	2.02	1.98
Maximum diameters of circles (m)	6.17	6.10	5.25	5.75	6.94	7.12	6.77	5.18	11.53
Mean nearest-neighbor distance (m)	9.98	9.46	9.78	9.35	9.15	9.14	9.64	11.05	12.36
% with 6 corners of Voronoi tiles	45	53	43	49	49	46	43	49	43
Mean number of corners of Voronoi tiles	5.98	5.96	5.97	5.95	5.95	5.97	5.92	5.98	5.98
PCF, highest *g*-value	1.5	1.5	1.5	1.4	1.4	1.4	1.4	1.9	1.5
PCF, 1st range of negative correlation (m)	9.0	8.5	8.5	8.0	8.5	8.0	9.0	9.5	11.5
MCF, 1st range of negative correlation (m)	10.0	9.5	8.5	10.0	8.0	9.5	9.0	9.5	13.0

PCF = pair-correlation function, MCF = mark-correlation function. The right column shows results for the one exemplary FC plot ‘G1’ from Namibia, published in Getzin et al. (7).

Table S2. Soil analysis of gap center, gap periphery, and matrix.

	Gap center	Gap periphery	Matrix
PSD (%)			
Clay (< 2 µm)	**18.13**	**12.10**	**6.53**
Fine Silt (2-20 µm)	**38.88**	**23.89**	**13.86**
Coarse Silt (20-50 µm)	**6.73**	**4.34**	**3.67**
Sand (50-2000 µm)	**36.26**	**59.66**	**75.94**
SOM (%)	0.93	0.61	0.50
pH	5.02	5.85	5.87
EC (µs/cm)	**203.07**	**77.90**	**59.30**
Mineralogy (%)			
Quartz	69.67	69.33	63.33
Microcline	16.67	22.00	28.33
Iron Oxide	6.00	3.83	4.33
Kaolinite	7.67	4.67	3.67
Major Elements (%)			
Al	8.75	7.39	6.58
Ca	0.22	0.08	0.06
Fe	5.70	4.34	3.66
K	2.61	3.04	3.24
Mg	0.17	0.12	0.10
Na	0.11	0.13	0.15
Si	32.93	34.99	36.00
Ti	0.46	0.38	0.33
Hydrology			
I_i (mm/min)	**0.07**	**0.45**	**0.70**
I_f (mm/min)	**0.03**	**0.15**	**0.30**
k (mm/s)	**0.001**	**0.08**	**0.05**

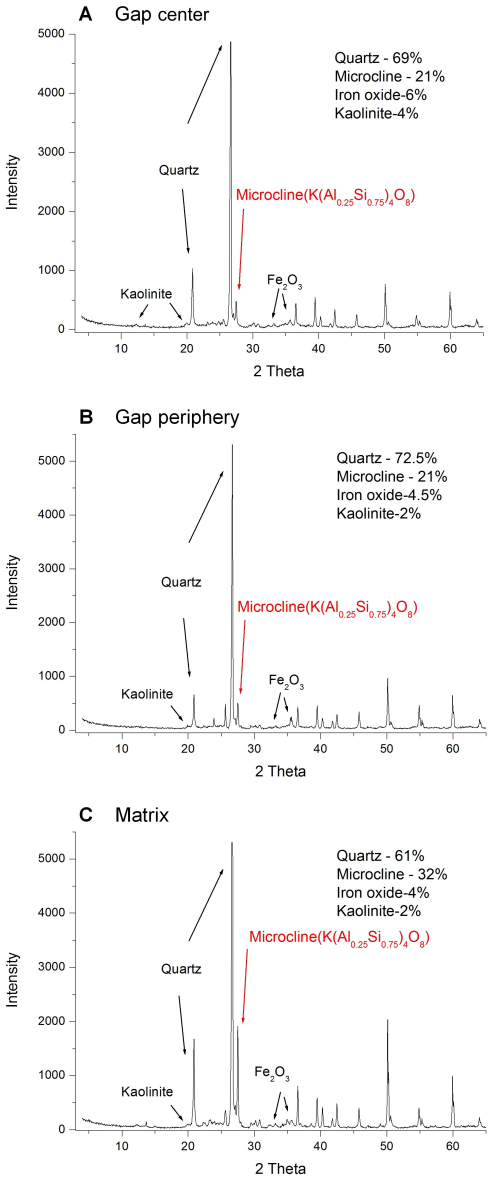

Physical and chemical properties of the soil at the gap center, gap periphery, and matrix: PSD = particle size distribution; SOM = soil organic (carbon) matter; EC = electrical conductivity; I_i = initial infiltration; I_f = final infiltration; k = hydraulic conductivity. Significant differences were determined for $P \leq 0.05$. Differences at this level among the gap center, gap periphery, and vegetation matrix were found only in the PSD, EC, and in the hydrological parameters I_i, I_f, k (bold numbers). Right side of the panel: graphical example of mineralogical composition for the field plot L1. Phase analysis of the samples performed by the X-ray powder diffraction (XRPD). Theta represents the scanning angle used for the phase identification. The intensity mode represents the amount of each identified component.

The PSD results show that the soils in the studied area range from loamy-sand to silt-loam textures. The soil in the gap center contains significant higher amounts of clay (< 2 µm) compared with the matrix soil. The soil is somewhat acidic with a pH value below 6 with no significant differences ($P \leq 0.05$) among the center, periphery, and matrix. The obtained electrical conductivity (EC) (µs/cm) is relatively low for soils (from 59.3 in the matrix to 203.07 in the gap center), but indicates a significant ($P \leq 0.05$) slightly higher accumulation of soluble salts in the gap center. The mineralogy is composed mostly of minerals that are

typical for metamorphic rocks, quartz, and microcline (KAlSi3O8). The presence of these minerals as well as the clays (e.g. Kaolinite) found in the studied soils is reflected in the elemental analysis. Al, Fe, K, and Si are the major elements with no significant difference among the three environments. The results of the soil hydrology show significantly higher infiltration (I_i and I_f) and higher conductivity (k) rates in the vegetation matrix compared to the gap center.

Table S3. Recordings of gap sizes and termite/ant signs at three field sites.

Gap number	Mean	Number	Number	Gap number	Mean	Number	Number
Field site C1	gap diameter	termite signs	ant signs	**Field site L2**	gap diameter	termite signs	ant signs
1	4.90	3	0	31	3.45	0	0
2	4.75	0	0	32	5.30	0	0
3	3.35	0	0	33	4.95	0	0
4	3.75	2	0	34	5.10	0	0
5	4.90	0	0	35	5.20	0	0
6	3.25	0	0	36	4.25	0	0
7	3.55	0	0	37	5.65	1	0
8	3.80	1	0	38	6.00	0	1
9	3.50	0	0	39	4.90	1	0
10	3.85	1	0	40	4.25	1	0
11	2.50	4	0	41	4.25	1	0
12	3.25	0	0	42	4.80	2	0
13	2.75	3	0	43	5.20	0	0
14	2.95	0	0	44	3.70	0	0
15	5.70	1	0	45	3.85	0	0
Field site L1							
16	4.40	0	0				
17	3.80	2	0				
18	4.30	3	0				
19	4.60	4	1				
20	2.20	2	1				
21	4.45	0	0				
22	3.95	0	0				
23	4.40	4	0				
24	3.45	3	1				
25	3.00	0	1				
26	4.00	3	0				
27	3.50	0	0				
28	4.65	2	1				
29	4.05	0	0				
30	4.70	6	0				

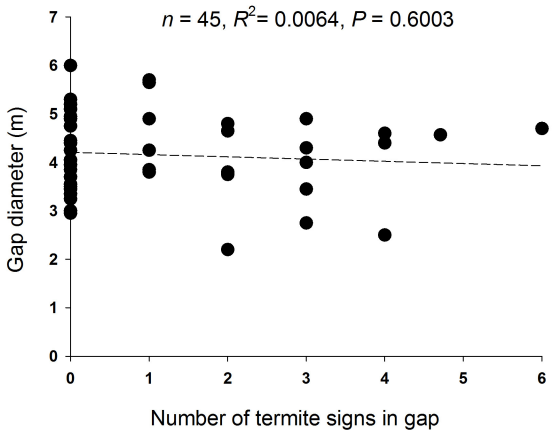

The proportion of gaps with termite signs were very variable in the field sites C1, L1, and L2. This large variability is also reflected by the aggregated distributions of the termite signs in the burnt field plot C2 where only 50 termite signs were found inside and partly outside a total of 328 fairy circles (see Fig. 5). While ant signs were more common on this burnt site C2, they were very rare or absent at the field sites C1, L1, and L2. The diagram shows the correlation between the diameter of gaps and the number of found termite signs in the gaps. The R^2 and dashed line show the standard linear regression fit based on the mean in the distribution of gap diameters. The low R^2-value indicates that the amount of termite activity did not correlate with gap size. Note that the field-measured mean gap diameter in the sites C1, L1, and L2 was overall 4.16 m (measurements taken at the larger two sides, accounting for asymmetric gap shape) while it was 3.73 m based on aerial image analysis (Table S1).

Table S4. A list of model parameters, their units, descriptions, and numerical values.

Parameter	Units	Description	Value
K	Kg/m^2	Maximum standing biomass	0.666
Q	Kg/m^2	Biomass reference value beyond which infiltration rate under a patch approaches its maximum	1.2
M	yr^{-1}	Rate of biomass loss due to mortality and disturbances	2
A	yr^{-1}	Infiltration rate in fully vegetated soil	120
N_W	yr^{-1}	Soil water evaporation rate	1.5
N_H	yr^{-1}	Surface water evaporation	4.5
E	m^2/Kg	Root's augmentation per unit biomass	1.5
Λ	$m^2/(Kg{\cdot}yr)$	Biomass growth rate per unit soil water	0.03
Γ	$m^2/(Kg{\cdot}yr)$	Soil water consumption rate per unit biomass	14
D_B	m^2/yr	Seed dispersal coefficient	0.1
D_W	m^2/yr	Transport coefficient for soil water	2.5
D_H	$m^4/(Kg{\cdot}yr)$	Bottom friction coefficient between surface water and ground surface	4
P	$Kg/(m^2{\cdot}yr)$	Precipitation rate	variable
R_W	–	Soil water evaporation reduction due to shading	0.3
R_H	–	Surface water evaporation reduction due to shading	0.8
f	–	Infiltration contrast between bare soil and vegetated soil	0.01

Table S5. Dimensionless quantities and the relations to their dimensional counterparts.

Quantity	Scaling	Quantity	Scaling
b	B/K	γ	$\Gamma K/M$
w	$W\Lambda/M$	p	$P\Lambda/M^2$
h	$H\Lambda/M$	δ_w	D_W/D_B
q	Q/K	δ_h	$D_H M/(D_B\Lambda)$
v_w	N_W/M	t	TM
v_h	N_H/M	x	$X(M/D_B)^{1/2}$
α	A/M	y	$Y(M/D_B)^{1/2}$
η	EK		

Supporting References

1. Gilad E, von Hardenberg J, Provenzale A, Shachak M, Meron E (2007) A mathematical model of plants as ecosystem engineers. *J Theor Biol* 244(4):680-691.
2. Stewart AD, Anand RR (2014) Anomalies in insect nest structures at the Garden Well gold deposit: Investigation of mound-forming termites, subterranean termites and ants. *J Geochem Explor* 140:77-86.
3. Noble J, Diggle P, Whitford W (1989) The spatial distributions of termite pavements and hummock feeding sites in a semi-arid woodland in eastern Australia. *Acta Oecol-Oec Gen* 10:355-376.
4. Jouquet P, Traore S, Choosai C, Hartmann C, Bignell D (2011) Influence of termites on ecosystem functioning. Ecosystem services provided by termites. *Eur J Soil Biol* 47(4):215-222.
5. Watson JAL, Lendon C, Low BS (1973) Termites in mulga lands. *Trop Grasslands* 7:121-126.
6. Schultheiss P, Cheng K (2013) Finding food: outbound searching behavior in the Australian desert ant Melophorus bagoti. *Behav Ecol* 24(1):128-135.
7. Getzin S*, et al.* (2015) Adopting a spatially explicit perspective to study the mysterious fairy circles of Namibia. *Ecography* 38(1):1-11.